Blue Order/Disorder Janus-Type TiO_2 Nanoparticles for Enhanced Photocatalytic Hydrogen Generation

Liangsheng Hu,[a] Yong Li,[a] Weiran Zheng,[a] Yung-Kang Peng,[b] Shik Chi Edman Tsang,[b] Lawrence Yoon Suk Lee,[a,] and Kwok-Yin Wong[a,]**

[a] Department of Applied Biology and Chemical Technology and State Key Laboratory of Chemical Biology and Drug Discovery, The Hong Kong Polytechnic University, Hung Hom, Kowloon, Hong Kong SAR, China

[b] Wolfson Catalysis Centre, Department of Chemistry, University of Oxford, Oxford, OX1 3QR, UK

***Corresponding Authors:** lawrence.ys.lee@polyu.edu.hk (L. Y. S. Lee);

kwok-yin.wong@polyu.edu.hk (K.-Y. Wong)

Abstract

Photochemical hydrogen generation from water is a promising solution to concurrently tackle energy and environmental problems. However, the solar-to-hydrogen conversion efficiencies of most photocatalysts are still unsatisfactory due to two major limiting factors: the non-ideal band structure of photocatalysts and the fast recombination of photo-generated charge carriers. Herein, we report a Janus-type TiO_2 heterojunction consisting of ordered blue-anatase and disordered black-rutile phases fabricated by the magnesiothermic reduction process. In this process, the surface enthalpy difference of rutile and anatase phases in P25-TiO_2 allows the phase-selective reduction to afford novel blue order/disorder Janus heterostructure. The joint effect of the improved light absorption and charge separation by disordered black-rutile phase and high catalytic activity of ordered blue-anatase phase, as well as the morphological advantage over order@disorder core-shell structures, significantly enhances the photocatalytic hydrogen production rate to 1.56 mmol $h^{-1}g^{-1}$ (11.53 mmol $h^{-1}g^{-1}$ with ~1 wt% Pt), which delivers 13-fold enhancement from the pristine P25-TiO_2.

Keywords: photocatalytic hydrogen evolution; black TiO_2; Janus-type heterojunction; magnesiothermic reduction; disorder engineering

1. Introduction

Photocatalysis driven by earth-abundant semiconductors is one of the prominent strategies that offer a green and sustainable solution to various energy- and environment-related challenges.[1] Among numerous semiconductors, titanium dioxide (TiO_2) is considered as one of the most promising candidates and has been widely studied for pollutant degradation,[2, 3] dye-sensitized solar cells,[4, 5] self-cleaning coatings,[6] photocatalytic carbon dioxide reduction,[1, 7, 8] photocatalytic hydrogen evolution,[1, 9-12] photoelectrochemical water splitting,[13, 14] and other applications[15-18] due to its relatively high photosensitivity, low toxicity, low cost, earth abundance, and excellent chemical/photochemical stability. However, the large electronic bandgap of TiO_2 (*ca*. 3.0 eV for rutile and 3.2 eV for anatase),[19] limits their light absorption to the ultraviolet (UV) region ($\lambda \leq$ 387.5 nm), which accounts for less than 5% of the solar spectrum. Over the past decade, much effort has been devoted to narrow the bandgap of TiO_2 in order to extend its optical response towards the visible and infrared light and thus enhance the efficiency of solar energy as well as the photocatalytic activities.[20] Doping TiO_2 with foreign elements, both metals and non-metals, has been extensively explored by means of inserting impurity levels in the forbidden band of TiO_2.[21-25] In particular, non-metal doping[23-25] has attracted a great deal of attention. Nevertheless, the effect of doping has been controversial owing to the possibility that the dopant, as an impurity, could also serve as a recombination center for the photo-generated electrons and holes, consequently lowering the photocatalytic efficiency.[23]

Very recently, Mao *et al*. made a significant breakthrough in increasing the solar absorption of TiO_2 nanoparticles by hydrogenating white TiO_2 to black TiO_2 under high pressure.[26] Different from the traditional element doping method, this novel blackening strategy involves the formation of disordered surface layers on TiO_2, which not only creates mid-gap states in the forbidden band

but also the blue shift of valence band (VB) edge.[27] As a result, the optical absorption range of the core-shell order@disorder TiO_2 expands from UV to visible and near infrared light (~1,200 nm) and the bandgap shrinks from 3.3 to 1.0 eV. In addition, such black TiO_2 showed a substantial enhancement in the photoactivity toward hydrogen evolution from water under simulated solar irradiation. This pioneering discovery sparked a huge attention in black TiO_2 nanomaterials and further studies on fabricating black TiO_2 under vacuum or reduced pressure have followed. Heating the pristine TiO_2 under reduced pressure introduces Ti^{3+} and/or oxygen vacancies into the TiO_2 lattice and changes white TiO_2 to different colors, such as yellow, blue, gray, and black. For example, Li *et al*. fabricated yellow and black rutile TiO_2 nanowires by hydrogenating TiO_2 under ambient hydrogen pressure at different temperatures.[28] Qiu *et al.* also synthesized blue rutile TiO_2 by treating pristine rutile TiO_2 powder at 450 °C for 1 h under a 40 bar pressure of hydrogen.[29] Yu *et al.* reported that the hydrogenation of anatase TiO_2 under an atmospheric hydrogen flow at 600 °C for 10 h yields grey TiO_2.[30] Black P25-TiO_2 was prepared by Lu *et al*. via a high-pressure (35 bar) hydrogenation of Degussa P25 at room temperature, and the color change of treated sample over time was also studied.[31] In addition, inspired by the idea of reducing white TiO_2 to black TiO_2, many other reducing reagents such as Al,[32, 33] Mg,[34, 35] $NaBH_4$,[36] and N_2H_4[37] were successfully employed to prepare black TiO_2.

Although the highly enhanced performance has been demonstrated on black TiO_2, the engaged photocatalytic mechanism is still somewhat contentious. On one hand, photocatalysts are generally expected to be highly crystalline to minimize the detrimental recombination of photo-generated charge carriers; the large number of vacancies and/or defects in the black outer layers (disordered/amorphous layers) of TiO_2 is normally considered to hamper the separation of photo-excited carriers.[38] On the other hand, the black layer of TiO_2 can absorb a wider range of solar

spectrum up to 1,200 nm. Liu *et al*. hypothesized that the localized mid-gap states in the disordered surface are beneficial for the spatial separation of photo-excited carriers, and that accounts for the high photocatalytic efficiency.[39] Usually, almost all the black TiO_2 samples fabricated by conventional gas phase, high temperature, and high-pressure reduction strategies have the order@disorder core-shell structure due to the disordering process that commences from the outer surface layer toward the core. The highly crystalline and catalytically active cores are often completely encased by the low-activity disordered/amorphous shells and hence cannot contact the substrate molecules.[38] Such dilemmatic situation of the core-shell structures can be resolved by an order/disorder Janus-type structure that can extend the light absorption without compromising the charge carrier recombination. Herein, a new controlled magnesiothermic reduction (MTR) method is developed to produce an order/disorder Janus-type TiO_2 nanocatalyst which consists of ordered blue-anatase and disordered black-rutile phases. In this process, the rutile and anatase phases of commercial P25-TiO_2 are reduced to different degrees at a certain temperature due to their difference in the surface enthalpy of reaction. The obtained order/disorder Janus architecture shows approximately 1,300% enhancement in photocatalytic hydrogen production compared to the pristine P25-TiO_2. The excellent performance could be ascribed to the synergetic effect of two phases; the disordered black-rutile phase broadens the light absorption range as well as boosts the separation of charge carriers, while the ordered blue-anatase phase keeps the high catalytic activity.

2. Experimental Section

2.1. Chemicals

Three kinds of commercial TiO_2 nanopowders, namely anatase TiO_2 (A-TiO_2, 99.7%), rutile TiO_2 (R-TiO_2, 99.9%), and P25-TiO_2 (4:1 anatase : rutile TiO_2, 99.5%) with BET specific surface areas

of 45~60 m^2 g^{-1}, hydrochloric acid, chloroplatinic acid hexahydrate ($H_2PtCl_6 \cdot 6H_2O$, 37.5% Pt basis), and triethanolamine (TEOA) were obtained from Sigma-Aldrich. Magnesium powder was purchased from Unichem Laboratories Ltd. All chemicals were used as received without further purification.

2.2. Synthesis of Mg-reduced A-TiO_2, R-TiO_2, and P25-TiO_2

The magnesiothermic reduction (MTR) method was engaged to treat the commercial TiO_2 nanopowders to give the reduced TiO_2 samples of different colors. Typically, 30 mg of Mg powder was thoroughly mixed with 200 mg of TiO_2 nanoparticles (A-TiO_2, R-TiO_2, or P25-TiO_2) by grinding them using a mortar in the air for 10 min. The mixture was then transferred into a stainless steel unsealed can and placed at the center of a quartz tube in a horizontal rapid thermal processing furnace. The reaction system was purged with high purity argon (99.999%) three times to remove any residual oxygen and/or moisture. The can was heated to 500 to 600 °C at a rate of 60 °C min^{-1} and maintained at the desired temperature for 30 min under Ar flow (50 standard cubic centimeters per minute, SCCM) and then cooled to 100 °C within 20 min. The mixture was then washed with the excess amount of 2 M HCl under stirring for overnight to remove the byproduct (MgO), and the product was rinsed with sufficient amount of Milli-Q water and ethanol several times to remove the acid and dried at 150 ºC in a vacuum oven overnight. The obtained TiO_2 samples are denoted as A-X, R-X, and P25-X, where X is the reaction temperature.

2.3. Synthesis of P25/Pt and P25-575/Pt

Pt nanoparticles (*ca.* 1.0 wt%) were loaded on P25 and P25-575 *via* photoreduction. In a typical process, 100 mg of P25 or P25-575 powder and 2.7 mg of $H_2PtCl_6 \cdot 6H_2O$ were added in 30 mL water containing 10 vol.% TEOA in a 50 mL sealed round-bottom quartz flask. The reaction vessel was then mixed under ultrasonication for 30 min, subsequently bubbled with Ar gas for 30 min

prior to the irradiation under a Newport solar simulator (Xe lamp, 150 W, 100 mW cm^{-2}) with continuous stirring for 3 h. The samples deposited with Pt (P25/Pt and P25-575/Pt) were filtered out and washed with water and dried at 150 °C in a vacuum oven for 12 h.

2.4. Characterization of the materials

The structure and morphology of samples were obtained from a scanning transmission electron microscopy (TEM, JEOL JEM-2100F). Crystallographic phases of samples were identified using the X-ray diffraction (XRD, Bruker D2 PHASER) patterns collected with a diffraction angle 2θ ranging from 10 to 80° at a scan rate of 10° min^{-1}. The Raman spectra were recorded on a Renishaw 2000 Raman spectrometer. Continuous-wave electron paramagnetic resonance (EPR) spectra were obtained using an X-band (9.4 GHz) Bruker EMX EPR spectrometer at 25 ºC. The composition, chemical states, and valence band (VB) spectra of the samples were determined by X-ray photoelectron spectroscopy (XPS, ESCALab 250). The ultraviolet–visible-near infrared (UV-Vis-NIR) absorption spectra were collected using UV–vis absorption and diffuse reflectance spectroscopy on a Cary 4000 UV-visible spectrophotometer equipped with an integrating sphere for diffuse and total reflection measurements. Photoluminescence (PL) spectra were recorded on a PTI QM-TM (Photon Technology International) fluorescence spectrophotometer with an excitation wavelength of 330 nm.

2.5. Photocatalytic reaction

For photocatalytic hydrogen evolution reaction (HER), 2 mg of catalyst was dispersed in an aqueous solution (20 mL) containing 10 vol.% TEOA as sacrificial agents in a sealed 50 mL round-bottom quartz flask. After sonicating for 20 min, the sample was degassed by bubbling with Ar for 30 min. The sample solution was irradiated with a Newport solar simulator (Xe lamp, 150 W, 100 mW cm^{-2}) under continuous stirring. To reveal the visible light photoactivity of the prepared

samples, HER performance was estimated under visible light irradiation using a 400 nm cut-off filter to the solar simulator source. The amount of produced H_2 was analyzed by an Agilent 7890B gas chromatography (GC) system with N_2 as carrier gas and a thermal conductivity detector. Cyclic HER test was conducted to examine the durability of sample by purging the reaction flask with Ar gas for 30 min after every 3-hour HER reaction under light irradiation. The apparent quantum efficiency (AQE) for photocatalytic H_2 production was estimated using a 300 W Xe lamp (Aulight, CEL-HXUV300) equipped with 365, 400, 420, and 520 nm bandpass filters. The AQE of photocatalytic H_2 production was calculated according to Eq. (1):

$$\mathrm{AQE} = \frac{\text{Number of } H_2 \text{ molecules} \times 2}{\text{Number of incident photons}} \times 100\ (\%) \qquad (1)$$

2.6. Photoelectrochemical analysis

Electrochemical impedance spectroscopy (EIS) and photocurrent measurements were carried out on a CHI760E potentiostat (CH Instruments) using a standard three electrode system with a Pt foil and saturated calomel electrode (SCE) as the counter and reference electrodes, respectively. The glassy carbon electrode (GCE, d = 3 mm) and indium tin oxide (ITO, area = 1 cm^2) coated with photocatalyst were engaged as the working electrode for EIS and photocurrent measurement, respectively. To prepare the working electrodes, catalyst inks (10 mg mL^{-1} for EIS and 100 mg mL^{-1} for photocurrent measurement) were first prepared in 75 % ethanol solutions containing 0.5 % Nafion (DuPont), and drop-cast onto GCE (5 μL for EIS) and ITO (15 μL for photocurrent measurement),[40, 41] followed by drying in air. 1.0 M NaOH was employed as the supporting electrolyte. A 300 W Xe lamp, with and without a cut-off filter (λ > 400 nm), was used as the irradiation source. Photocurrent measurements were performed at a 0.4 V bias potential *vs.* SCE. EIS tests were conducted in the frequency range of 100 kHz and 0.1 Hz with an AC perturbation of 10 mV.

3. Results and discussion

3.1. Reduced A-TiO_2 and R-TiO_2

The surface enthalpy of anatase-phase TiO_2 (A-TiO_2) is known to be lower than that of rutile-phase TiO_2 (R-TiO_2)[42, 43] and it is therefore easier to reduce R-TiO_2 to TiO_{2-x} under the same reaction conditions. By carefully tuning the reaction conditions, it is possible to selectively reduce/disorder only the R-TiO_2 in P25-TiO_2 to a disordered phase while keeping the A-TiO_2 unchanged, which will lead to the formation of order/disorder Janus-type TiO_2 nanostructure. In order to establish the reaction conditions such that only the R-TiO_2 phase in P25-TiO_2 would be reduced, the MTR progress of A-TiO_2 and R-TiO_2 was thus separately correlated to their color evolution as reference. The pristine A-TiO_2 and R-TiO_2 were reduced to different degrees by treating them at a temperature between 500 and 600 °C for 30 min. The digital photos of untreated and reduced A-TiO_2 and R-TiO_2 are shown in **Fig. S1** and **S2**, respectively. After the MTR treatment at 500 °C, the color of pristine A-TiO_2 turns from white to dull yellow. The increases in reaction temperature to 525, 550, and 575 °C yield the reduced A-TiO_2 with dark yellow, blue, and dark blue color, respectively. With the reduction temperature further increased to 600 °C, A-TiO_2 is reduced to black color (**Fig. S1f**). A similar gradual color change from white to black is also observed from R-TiO_2 as the reduction temperature is raised (**Fig. S2**). In general, the color of R-TiO_2 is darker than the A-TiO_2 treated under the same reaction conditions. For example, R-575 is dark black while A-575 is blue, suggesting that at the reduction temperature 575 ºC, R-575 could be disordered[26] but A-575 still retains the ordered crystal structure. The XRD patterns of A-TiO_2 and R-TiO_2 reduced under various conditions are given in **Fig. 1**. All the diffraction peaks of pristine and reduced A-TiO_2 samples match well with those of anatase TiO_2 (JCPDS Card no. 21-1272). The peak intensities, however, gradually weaken with the treatment temperature. In the pattern of A-600, all the

diffraction peaks corresponding to anatase TiO_2 completely vanish, while four new peaks emerge at 37.1°, 43.1°, 62.7°, and 75.2°, which can be attributed to the (111), (200), (220), and (311) planes of $TiO_{0.89}$ (JCPDS Card no. 78-0720). It is clear that the elevated reaction temperature lowers the crystallinity of TiO_2 as more defects are introduced. The R-TiO_2 samples also exhibit the similar trend as A-TiO_2 (**Fig. 1b**), however, the disappearance of rutile peaks occurs at a lower temperature of 575 °C. We used Raman spectroscopy to further gather insights into the structures of reduced A-TiO_2 and R-TiO_2 and the results are summarized in **Fig. S3**. The characteristic Raman bands of anatase TiO_2 (three E_g at 144, 198, and 641 cm^{-1}, one B_{1g} at 398 cm^{-1}, and one A_{1g} at 519 cm^{-1})[44] are evident for all A-TiO_2 samples except for A-600. Compared to pristine A-TiO_2, the reduced samples exhibit blue shifts of the strongest E_g band at *ca*. 144 cm^{-1}, as well as the peak broadening with reduced intensity. This phenomenon is attributed to the non-stoichiometric structure due to the oxygen deficiency/vacancy created by surface modification.[26, 28, 32, 45] The peaks observed for R-TiO_2 samples at 243 cm^{-1} (second-order Raman scattering), 450 cm^{-1} (E_g), and 612 cm^{-1} (A_{1g}) are the characteristic Raman bands of rutile TiO_2,[46] all of which disappear after the treatment at or above 575 °C. Another noticeable observation is the large red shift and broadening of the peak at 450 cm^{-1} which are related to the oxygen non-stoichiometry of reduced rutile TiO_2.[47, 48]

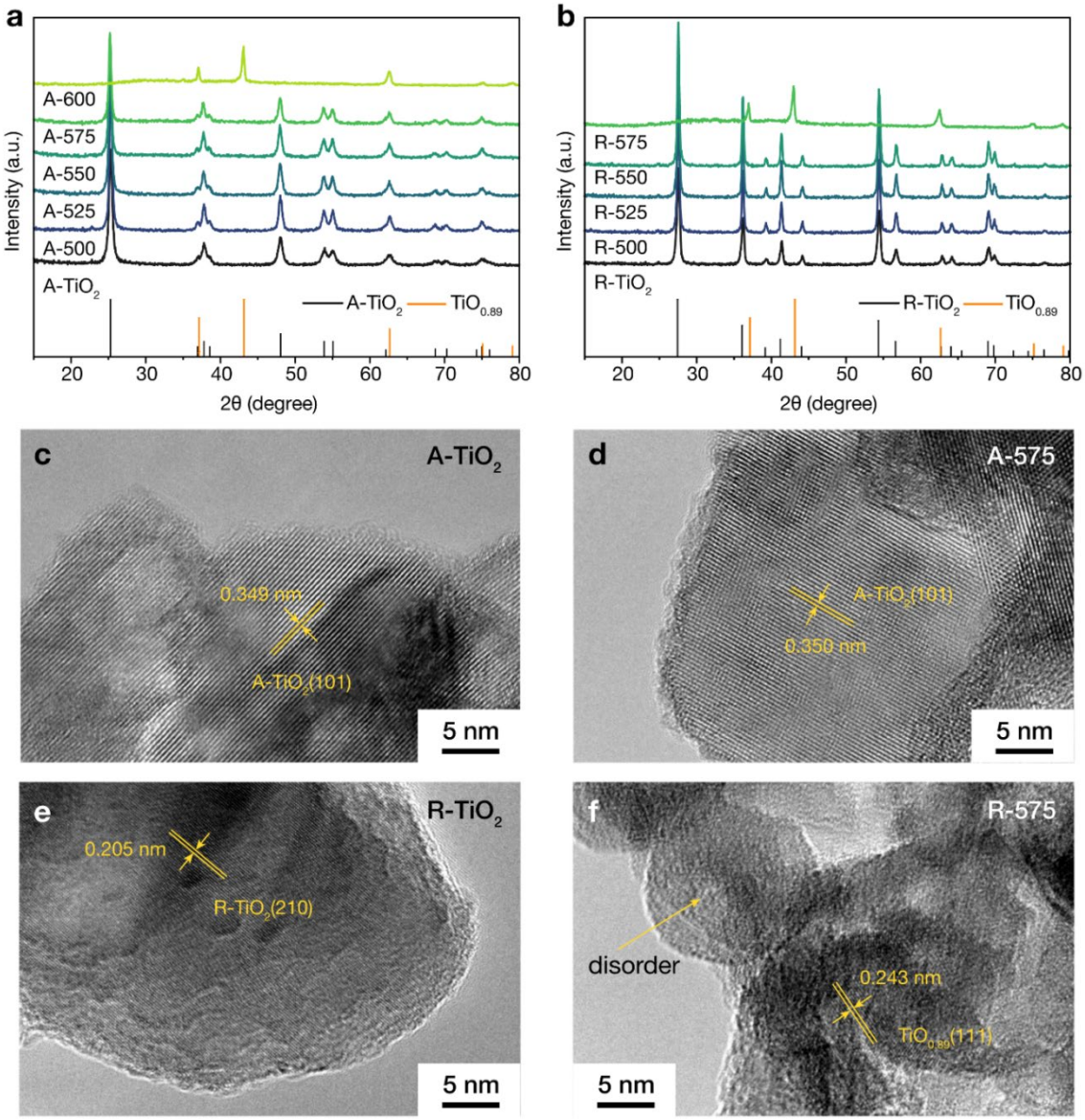

Fig. 1. XRD patterns of (a) pristine and reduced A-TiO_2 samples at 500 to 600 °C and (b) pristine and reduced A-TiO_2 samples at 500 to 575 °C. HR-TEM images of pristine (c) A-TiO_2 and (d) R-TiO_2, and the reduced (e) A-575 and (f) R-575 at 575 °C by MTR.

To reveal the structure of reduced TiO_2 samples, high-resolution TEM (HR-TEM) was engaged and their typical images are presented in **Fig. 1c-f**, **S4**, and **S5**. Well-resolved (101) lattice planes with typical anatase *d*-spacing of *ca*. 0.350 nm are observable in the HR-TEM images of A-500, A-525, A-550, and A-575, indicating that their highly crystalline structures remain intact. Noticeably, a thin disordered layer (thickness = *ca*. 0.5 nm) is observed on the outer boundary of

A-575 (**Fig. 1d**). The reduction of A-TiO_2 at 600 °C turns most parts of crystal structure disordered, also forming a small amount of $TiO_{0.89}$, as shown in **Fig. S4f**. This agrees well with the XRD results. The HR-TEM images of R-TiO_2 samples (**Fig. S5**) also reveal the similar observations. The disordered layer, however, starts to appear from the reduction temperature of 550 °C, slightly lower than the case of A-TiO_2. The R-575 (**Fig. 1f**) exhibits mostly disordered structure with some obscure lattice fringes with a *d*-spacing of 0.243 nm, which can be ascribed to the interplanar spacing of the (111) plane of $TiO_{0.89}$. The Fast Fourier Transformation (FFT) image of R-575 (**Fig. S5g**) further confirms that it is fully disordered. The HR-TEM data are entirely consistent with the XRD and Raman spectroscopic results.

3.2. Mg-reduced P25-TiO_2

The reduction tests for A-TiO_2 and R-TiO_2 indicate that the reducibility of two crystalline phases is different, especially at 575 °C, most probably due to the different enthalpies of two phases. Commercial P25-TiO_2 nanoparticles with the mixed anatase and rutile phases were therefore treated by MTR at 575 °C in order to form a disordered-R/ordered-A heterostructure by selectively reducing/disordering rutile phase of P25-TiO_2. The white color of pristine P25-TiO_2 has changed to dark blue (**Fig. 2a**), which is hereby denoted as B-P25. The XRD pattern of pristine P25-TiO_2 corresponds well to the characteristic anatase TiO_2 (2θ = 25.5°, 37.8°, 48.1°, 53.9°, and 55.1°) and rutile TiO_2 peaks (2θ = 27.5°, 36.1°, 41.2°, and 54.3°, **Fig. 2c**). The B-P25, on the other hand, displays largely reduced rutile TiO_2 peaks with the unaltered anatase peaks. **Fig. 2d** is the Raman spectra of P25 and B-P25 collected to compare the structural differences. The Raman peaks located at 144 (E_g), 197 (E_g), 397(B_{1g}), 517 (A_{1g}), and 639 cm^{-1} (E_g) correspond to the anatase phase TiO_2, while the two weak peaks centered at 449 (Eg) and 610 cm^{-1} (A_{1g}) are attributed to the rutile phase TiO_2. From the spectra of B-P25, only anatase peaks are seen with the reduced intensities as well

as blue-shifted E_g peak (144 cm^{-1}), which indicates the production of surface oxygen deficiencies/vacancies.[49]

TEM analyses further reveal the surface microstructures of P25 and B-P25 TiO_2. The TEM images of P25 (**Fig. S6a** and **S6b**) and B-P25 (**Fig. S6c** and **S6d**) show that the particle sizes are similar (ranging from 20 to 35 nm), confirming no morphological changes by the MTR process. The HR-TEM image at the crystal interfaces of pristine P25-TiO_2 clearly displays a well-defined rutile-anatase interface (**Fig. 2e**) with the lattice spacings of 0.205 and 0.357 nm for the (210) planes of R-TiO_2 and the (101) planes of A-TiO_2, respectively. In contrast, the HR-TEM image of B-P25 (**Fig. 2f**) shows that R-TiO_2 is completely disordered while the microstructure of A-TiO_2 remains unchanged, forming a disorder (R-TiO_2)/order (A-TiO_2) heterojunction. Careful inspection of the disordered region in HR-TEM image (**Fig. S7**) identifies some obscure lattice fringes with a *d*-spacing of 0.126 nm, corresponding to the interplanar spacing of the (311) plane of $TiO_{0.89}$, which agrees well with the observation from R-575. However, the XRD pattern of B-P25 exhibits no signal assignable to $TiO_{0.89}$, most probably due to the low concentration of $TiO_{0.89}$ in B-P25. Based on TEM, XRD, and Raman data, a disorder/order Janus architecture can be confirmed (**Fig. 2b**). The UV-Vis diffuse reflectance spectra (DRS) of P25 and B-P25 (**Fig. 2g**) indicate that the MTR process broadens the absorption range of P25 from only the UV region to the near-infrared (NIR) region. The corresponding Tauc plots of P25 and B-P25 (**Fig. 2h**) support this with the narrower estimated bandgap energy of B-P25 (2.10 eV) than that of P25 (3.03 eV).

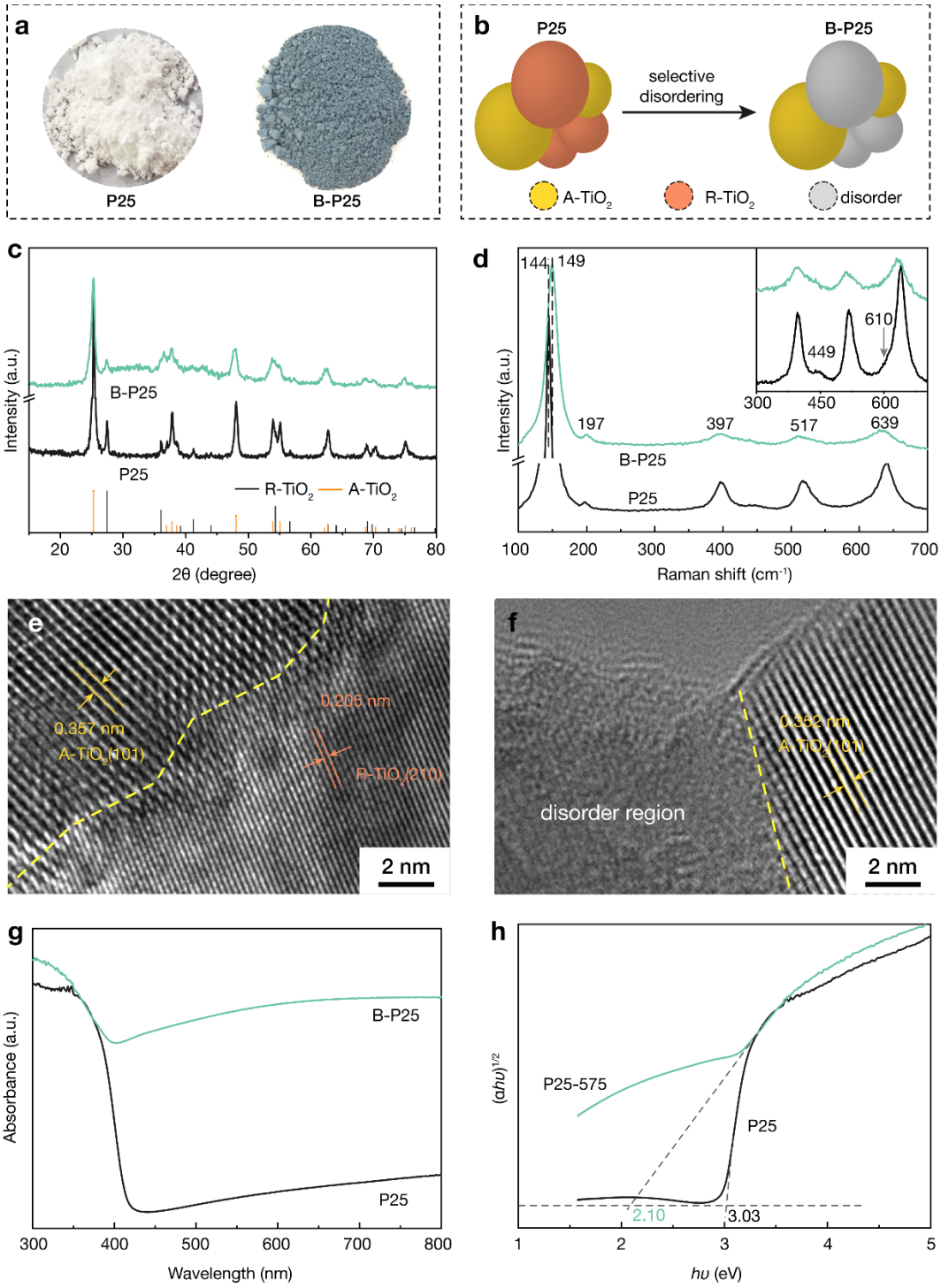

Fig. 2. (a) Digital photos of pristine P25 and B-P25. (b) Schematic illustration of the selective reduction/disordering of P25 to B-P25 nanoparticles. (c) XRD patterns, (d) Raman spectra of P25 and B-P25. HR-TEM images of (e) P25 and (f) B-P25. (g) UV-Vis absorption spectra and (h) the corresponding Tauc plots of P25 and B-P25 TiO_2.

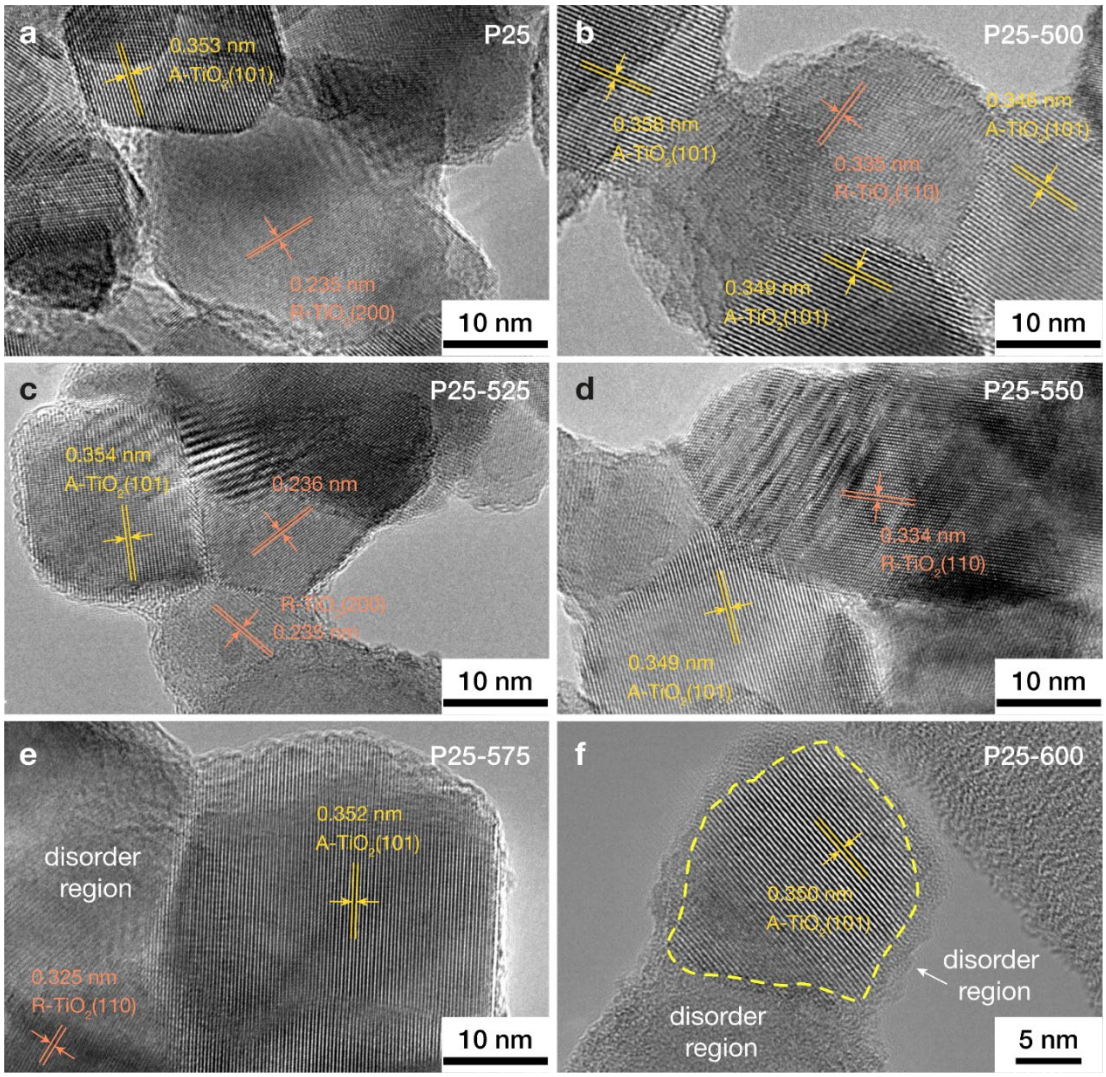

Fig. 3. HR-TEM images of (a) P25-TiO_2 and (b-f) P25-TiO_2 treated by MTR at 500 to 600 °C for 30 min.

The effect of MTR temperature on the crystal structure of P25-TiO_2 was investigated by varying the treatment temperature between 500 and 600 °C. From the HR-TEM images (**Fig. 3**), both lattice fringes corresponding to anatase and rutile phases are clearly seen from the pristine P25, as well as the samples treated at 550 ºC or lower. The P25-575, however, shows obvious order/disorder boundaries: the anatase phase TiO_2 is unchanged while the most parts of rutile TiO_2 are disordered (**Fig. 3e**). Moreover, the MTR process at 600 ºC further expands the disordered area, completely encompassing the anatase phase (**Fig. 3f**). This demonstrates that the A-TiO_2 and R-

TiO_2 phases in B-P25 are reduced/disordered to the different extents to yield an order/disorder heterojunction by simply controlling the reducing temperature.

3.3. Photocatalytic hydrogen evolution reaction

To evaluate the advantages of forming a Janus structure, the photocatalytic activities toward hydrogen evolution reaction (HER) were compared among P25 and the reduced P25 samples (**Fig. 4a**). Under simulated solar light irradiation, the HER rate of pristine P25 is merely 0.12 mmol h^{-1} g^{-1}, as expected for its large bandgap. The HER rate is increased to 0.25, 0.34, and 0.77 mmol h^{-1} g^{-1} with P25-500, P25-525, and P25-550, respectively, showing an increasing trend with the treatment temperature due to the enhanced light absorption of reduced P25 samples (**Fig. S8**). The photocatalytic HER rate reaches a maximum of 1.56 mmol h^{-1} g^{-1} with P25-575 (B-P25), which is 13.3 times higher than the pristine P25. Despite the smallest bandgap energy among all samples, the P25-600, however, exhibits the weakest photocatalytic activity (0.09 mmol h^{-1} g^{-1}), even lower than pristine P25. This may be correlated with the structure of P25-600, where the active anatase phase is surrounded by disordered phase, similar to order@disorder core-shell structure, which has an adverse effect on the photocatalytic HER.[38] A continuous 18-hour irradiation test on B-P25 shows that the volume of produced hydrogen linearly increases with the irradiation time, indicating its stability over long-term reaction (**Fig. S9**). In addition, we further conducted the cyclic HER tests to examine the durability of B-P25 sample.[41, 50] **Fig. 4b** shows steady HER rates during six 3-hour HER tests where Ar is purged before next run. TEM images (**Fig. S10**), XRD pattern (**Fig. S11a**), Raman spectrum (**Fig. S11b**), UV-Vis absorption spectrum (**Fig. S11c**), extinction coefficient (**Fig. S11d**), and XPS spectra (**Fig. S12**) collected after the cyclic photocatalytic reactions indicate that the morphology, crystal structure, phase composition, optical absorption, and chemical compositions of B-P25 are retained except for the slight drop of Ti^{3+} ratio compared

with the fresh B-P25, suggesting high chemical and structural stability as well as good reusability of the developed B-P25.

To further enhance the photocatalytic HER efficiency, Pt nanoparticles, a commonly used co-catalyst, were decorated on the surface of P25 and B-P25 by photoreduction. With *ca.* 1 wt% Pt loaded on B-P25 (B-P25/Pt), a hydrogen evolution rate of 11.53 mmol h^{-1} g^{-1} is achieved, which is 6.3-fold higher than that of platinized P25 (P25/Pt, **Fig. 4c**). Under visible light ($\lambda > 400$ nm) irradiation, the photocatalytic HER rate of the B-P25 (0.38 mmol h^{-1} g^{-1}) is 38-fold higher than that of P25 and 2.5-fold higher than that of P25/Pt (0.15 mmol h^{-1} g^{-1}). The HER rate of B-P25 under visible light can be further improved up to 3.52 mmol h^{-1} g^{-1} after loading the Pt nanoparticles. To evaluate the photon conversion efficiency, the wavelength-dependent apparent quantum efficiencies (AQEs) of B-P25 and B-P25/Pt were evaluated (**Fig. 4d**). The estimated AQEs of B-P25 are approximately 15.6 % at 365 nm, 2.3 % at 400 nm, and 0.7 % at 420 nm. However, the enhanced absorbance of B-P25 in the visible region (>420 nm) does not contribute to the AQE in photocatalytic HER. Similar phenomena have been reported,[26, 38, 51] showing the negligible contribution of expanded band tail to photoactivity. Platinizing the B-25 boosts the AQE values *ca*. 4 times. In particular, the AQE of B-P25/Pt at 520 nm is increased to 2.1 %, which indicates that B-P25 can effectively utilize visible light associated with Pt co-catalysts. In comparison with the photocatalytic performance of recently reported black TiO_2–based photocatalysts (**Table S1**), B-P25 and B-P25/Pt demonstrate outstanding photocatalytic activities that surpass most reduced/disordered TiO_2 nanostructures.[26, 36, 38, 52, 53]

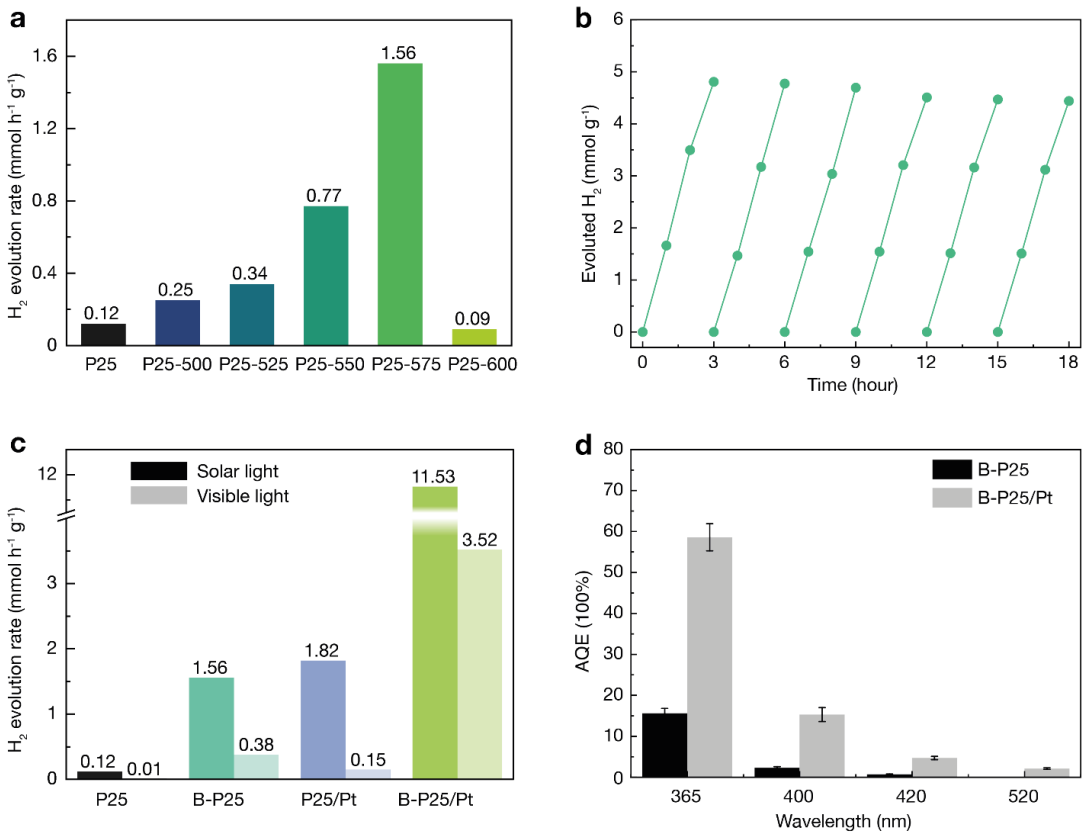

Fig. 4. (a) Comparison of photocatalytic HER rates among P25 and treated P25 samples. (b) Cyclic tests of the photocatalytic H_2 generation over B-P25. (c) Comparison of photocatalytic HER rates among P25, B-P25, P25/Pt, and B-P25/Pt samples under the irradiation of solar and visible lights. (d) Wavelength-dependent AQEs of photocatalytic H_2 production over B-P25 and B-P25/Pt.

3.4. Photocatalytic mechanism

As discussed in the previous sections, a Janus architecture consisting of ordered A-TiO_2 and disordered R-TiO_2 was successfully fabricated by a selective reduction/disordering process of P25. This nanostructure shows over 1,300 % enhancement in the photocatalytic HER rate compared with the untreated P25 TiO_2. To elucidate the factors for such highly enhanced HER photocatalytic activity, we also investigated the HER properties of single-phase A-TiO_2 and R-TiO_2 treated by MTR at different temperatures and further characterized the Janus B-P25 nanoparticles. As summarized in **Fig. S13**, A-TiO_2 and R-TiO_2 samples show a similar trend of HER rate on the treatment temperature, which improves with the treatment temperature until becomes disordered.

The optimized R-550 and A-575 record the HER rates of 0.49 and 0.61 mmol h^{-1} g^{-1}, respectively, which are much lower than that obtained from B-P25 (1.56 mmol h^{-1} g^{-1}). This clearly demonstrates the crucial role of order/disorder Janus structure for boosting the photocatalytic HER performance of B-P25. We then engaged the XPS to analyze the surface chemical composition of P25 and B-P25 and investigate the changes in surface states. The full XPS survey spectrum of B-P25 shows only Ti and O elements, confirming no Mg dopant is introduced during MTR treatment (**Fig. S14a**). The high-resolution XPS Ti 2p spectrum of P25 exhibits a pair of Ti $2p_{3/2}$ and $2p_{1/2}$ peaks at 459.1 and 464.7 eV, respectively, which is assigned to Ti^{4+} species (**Fig. 5a**, bottom). The Ti 2p spectrum of B-P25, on the other hand, displays three sets of Ti $2p_{3/2}$ and $2p_{1/2}$ peaks (**Fig. 5a**, top), where one new peak pair at 457.6 and 462.1 eV corresponds to Ti^{3+} species while the others centered at 455.5 and 460.2 eV are attributed to Ti^{2+} species.[54] The O 1s spectrum of P25 shows a single peak, whereas that of B-P25 exhibits three peaks (**Fig. S12b, top**). The peak at 530.5 eV, observed from both samples, is attributed to the lattice oxygen of TiO_2, while the peaks at 531.2 and 532.8 eV, observed only in B-P25, are assigned to Ti–OH and free –OH species, respectively.[55] The higher binding energy peaks in B-P25 suggest the presence of oxygen vacancies or surface defects,[34] which enable a wider range of light absorption. Electron paramagnetic resonance (EPR) is a very sensitive technique that can measure the unpaired electrons in paramagnetic species, and it has been widely used in the study of defects of paramagnetic centers.[56-58] We employed the EPR to confirm the existence of Ti^{3+} and oxygen vacancies on the sample surfaces. From the EPR spectra compared in **Fig. S14b**, very weak paramagnetic signals are observed at g = 2.002 and 2.004 from the spectrum of P25, which correspond to the electron trapped in defects such as oxygen vacancy (with one electron).[57, 58] In contrast, the same EPR signals appear *ca*. 53 times stronger in B-P25 (by comparing the integrated peak area), indicating more oxygen vacancies on

B-P25 surface. In addition, another single peak at g = 1.985 observed in B-P25 suggests Ti^{3+} defects generated during the MTR treatment.[56]

The UV-Vis DRS spectra of pristine and reduced A-TiO_2 and R-TiO_2 and the corresponding Tauc plots are given in **Fig. 5b** and **5c**, respectively. The bandgap energies of pristine A-TiO_2 and R-TiO_2 (3.25 and 3.03 eV) are reduced to 2.92 and 1.06 eV, respectively, upon the reduction at 575 °C. The positions of VB edge of samples were determined *via* VB-XPS spectra as shown in **Fig. 5d**. The pristine A-TiO_2 and R-TiO_2 show the VB maximum of 2.75 and 2.42 eV, respectively. Noticeably, the VB of A-575 shifts negatively by 0.05 eV with a tail appearing at 2.46 eV. The R-575 exhibits a main absorption onset at 2.21 eV accompanied by a band tail at 0.38 eV. This blueshift of the maximum energy level can be attributed to the presence of surface defects or oxygen vacancies/Ti^{3+}, resulting in the increased visible light absorption. The corresponding density of states (DOS) diagrams are illustrated in **Fig. S15**. The enhancement of photocatalytic activity of B-P25 is believed to arise from a large amount of Ti^{3+}/oxygen vacancies on the surface. Based on the Tauc plots and VB-XPS spectra of pristine and reduced TiO_2 samples,[38, 59, 60] the bandgap diagrams of both P25 and B-P25 are illustrated in **Fig.5e**, where the separation/transfer of photo-excited electrons (e^-) and holes (h^+) in P25 and B-P25 could be descripted as a type-II heterostructure. It has been reported that the sublattice distortion of Ti and O atoms can induce the blueshift of the VB energy state thus leading to reduced bandgaps and creating intermediate defect levels in black TiO_2.[26, 27, 59] The intermediate energy states could act as trapping or sinking center for photo-generated charge carriers.[27, 59] In this regard, the Janus-type order (A-TiO_2)/disorder (R-TiO_2) heterojunction in B-P25 can efficiently separate electron-hole pairs through a type-II band alignment in which the photo-generated electrons and holes flow to the conduction band (CB) of A-TiO_2 crystal and VB of disordered R-TiO_2, respectively. The black R-TiO_2 in B-P25 not only

enhances the visible light absorption but also suppresses the recombination of photoexcited electrons and holes.

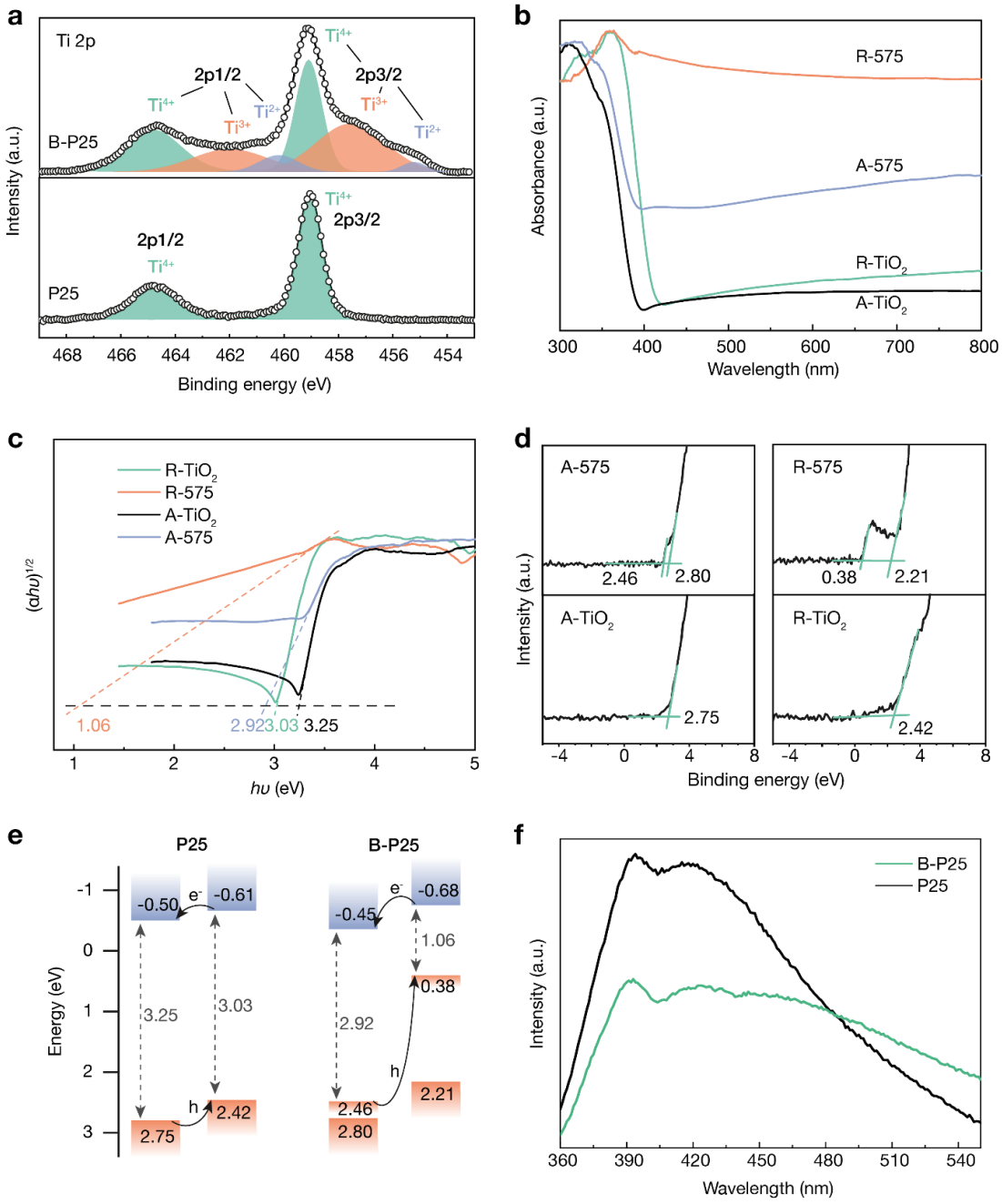

Fig. 5. (a) High-resolution XPS Ti 2p spectra of P25 and B-P25. (b) UV-Vis absorption spectra, (c) the corresponding Tauc plots, and (d) VB-XPS spectra of A-TiO_2, R-TiO_2, A-575, and R-575. (e) Proposed separation mechanism of photo-generated electrons (e^-) and holes (h^+), and calculated bandgap diagrams for P25 and B-P25. (f) PL spectra of P25 and B-P25.

To further confirm the transfer pathway of photo-generated charge carriers and gain the information on the active sites, we conducted a series of photoelectrochemical and electrochemical measurements with P25 and B-P25. Photoluminescence (PL) emission spectroscopy is a useful technique in revealing the separation efficiency of photo-generated electrons and holes since PL emission is associated with the recombination of charge carriers in semiconductors.[61, 62] As shown in **Fig. 5f**, both P25 and B-P25 display a strong emission peak in the wavelength range from 400 and 500 nm, while the PL emission intensity of B-P25 is considerably lower than that of P25, implying a lowered recombination rate of electrons-hole pairs in B-P25. In defect-engineered TiO_2, the oxygen vacancies/Ti^{3+} cause mid-gap states that act as strong photo-generated hole trapping sites, thus suppressing the recombination kinetics of electrons and holes.[26, 27, 59] This argument is further verified by photocurrent measurements and electrochemical impedance spectroscopy (EIS). **Fig. 6a** and **S16** are the transient chronoamperometry profiles of P25 and B-P25 recorded at a 0.4 V bias potential *vs.* SCE under UV-Vis and visible light irradiation, respectively. Compared with P25, B-P25 displays boosted on-off responses with the photocurrent density increased 3.8 and 4.7 times under UV-Vis and visible light illumination, respectively, suggesting apparently prompted interfacial charge transfer and photoelectric conversion capability.[40, 41] The Nyquist plots of P25 and B-P25 obtained from EIS (**Fig. 6b**) display a smaller semicircle for B-P25, revealing the higher charge mobility of B-P25 over P25.[60]

Moreover, another control experiment was carried out by depositing Pt nanoparticles (~1.0 wt%, **Fig. S17**) on the surface of P25 and B-P25 via *in situ* photoreduction of chloroplatinic acid. The TEM images in **Fig. 6c** and **6d** show that the Pt nanoparticles are randomly deposited on the surface of both anatase and rutile phases of P25. On the contrary, Pt nanoparticles in B-P25 are concentrated at the interfaces of anatase and disordered phases (**Fig. 6e** and **6f**), indicating electron-

rich nature of those sites for reduction reaction.[63] The Pt nanoparticles are rarely loaded on the surface of disordered R-TiO_2, indicating the photo-generated electrons mostly flow toward A-TiO_2.

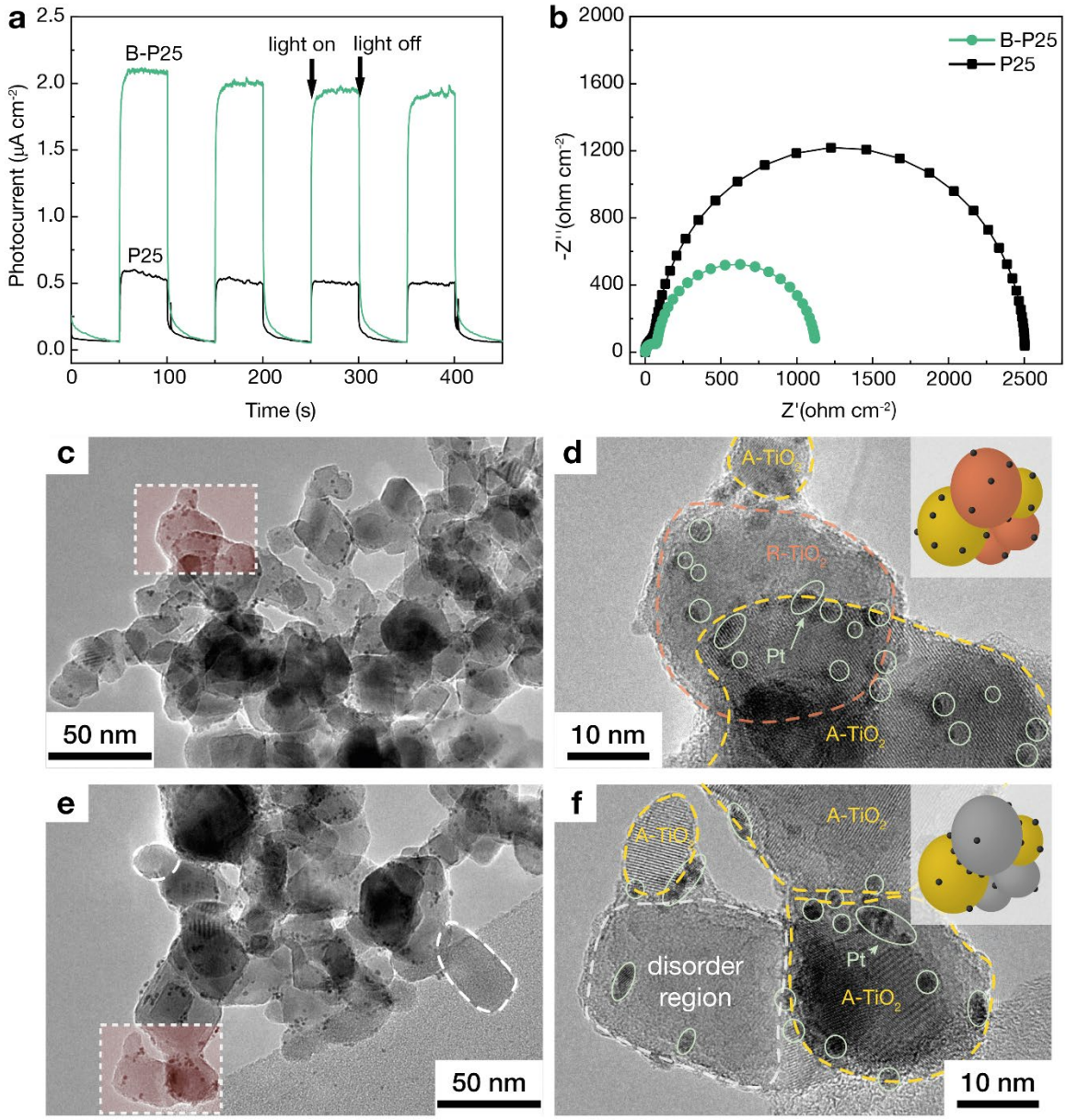

Fig. 6. (a) Photocurrent responses of P25 and B-P25 under UV-Vis light irradiation. (b) Nyquist plots of P25 and B-P25. TEM images of (c and d) P25/Pt and (e and f) B-P25/Pt. Insets in d and f are the schematic illustration of the morphologies where orange is R-TiO_2, yellow is A-TiO_2, grey is disordered TiO_2, and black is Pt nanoparticle.

4. Conclusions

In summary, a blue Janus-type TiO_2 nanostructure consisting of ordered anatase and disordered rutile was fabricated by a controlled magnesiothermic reduction method. In this process, the rutile and anatase phases of P25-TiO_2 were reduced to the different extents due to their different enthalpies of reaction. The XRD, TEM, Raman, and XPS results confirm the Janus-type structure of the P25 treated at 575 °C. The disordered black-rutile phase broadens the light absorption range as well as boosts the separation of charge carriers, leading to an improved photocatalytic HER rate of 1.56 mmol h^{-1} g^{-1} under the illuminated sun light without using any co-catalysts. This HER rate was further improved to 11.53 mmol $h^{-1}g^{-1}$ by loading *ca.* 1.0 wt% Pt nanoparticles as co-catalyst. The blue P25-TiO_2 exhibits over 1,300 % enhancement in photocatalytic activity compared to the pristine P25. The visible light photocatalytic activity of blue P25-TiO_2 is also substantially promoted, showing a HER production rate 38-times higher than that of P25. In addition, blue P25-TiO_2 shows high chemical and structural stability as well as good reusability.

Acknowledgements

The authors are thankful to Dr. Xiang Peng and Prof. Paul K. Chu of City University of Hong Kong for instrumental supports. This work is financially supported by the Innovation and Technology Commission of Hong Kong to the State Key Laboratory of Chemical Biology and Drug Discovery, The Hong Kong Polytechnic University. K.-Y.W. acknowledges the support from the Patrick S.C. Poon Endowed Professorship.

Appendix A. Supplementary data

Supplementary material related to this article can be found, in the online version, at doi: https:

References

1. Y. Ma, X. Wang, Y. Jia, X. Chen, H. Han and C. Li, *Chem. Rev.*, 2014, **114**, 9987-10043.

2. C. Liu, A.-Y. Zhang, Y. Si, D.-N. Pei and H.-Q. Yu, *Environ. Sci. Technol.*, 2019, **53**, 7641-7652.

3. J. Tian, Z. Zhao, A. Kumar, R. I. Boughton and H. Liu, *Chem. Soc. Rev.*, 2014, **43**, 6920-6937.

4. U. Bach, D. Lupo, P. Comte and J. Moser, *Nature*, 1998, **395**, 583.

5. M. Freitag, J. Teuscher, Y. Saygili, X. Zhang, F. Giordano, P. Liska, J. Hua, S. M. Zakeeruddin, J.-E. Moser, M. Grätzel and A. Hagfeldt, *Nat. Photonics*, 2017, **11**, 372-378.

6. S. Banerjee, D. D. Dionysiou and S. C. Pillai, *Appl. Catal. B Environ.*, 2015, **176**, 396-428.

7. X. Li, J. Yu, M. Jaroniec and X. Chen, *Chem. Rev.*, 2019, **119**, 3962-4179.

8. J. Jin, S. Chen, J. Wang, C. Chen and T. Peng, *Appl. Catal. B Environ.*, 2020, **263**, 118353.

9. Y. Hou, A. B. Laursen, J. Zhang, G. Zhang, Y. Zhu, X. Wang, S. Dahl and I. Chorkendorff, *Angew. Chem. Int. Ed.*, 2013, **52**, 3621-3625.

10. J. Pan, Z. Dong, B. Wang, Z. Jiang, C. Zhao, J. Wang, C. Song, Y. Zheng and C. Li, *Appl. Catal. B Environ.*, 2019, **242**, 92-99.

11. Y. Li, Y.-K. Peng, L. Hu, J. Zheng, D. Prabhakaran, S. Wu, T. J. Puchtler, M. Li, K.-Y. Wong, R. A. Taylor and S. C. E. Tsang, *Nat. Commun.*, 2019, **10**, 4421.

12. E. B. Clatworthy, S. Yick, A. T. Murdock, M. C. Allison, A. Bendavid, A. F. Masters and T. Maschmeyer, *J. Phys. Chem. C*, 2019, **123**, 3740-3749.

13. Y. Mi, L. Wen, R. Xu, Z. Wang, D. Cao, Y. Fang and Y. Lei, *Adv. Energy Mater.*, 2016, **6**, 1501496.

14. T. Zhou, J. Wang, S. Chen, J. Bai, J. Li, Y. Zhang, L. Li, L. Xia, M. Rahim, Q. Xu and B. Zhou, *Appl. Catal. B Environ.*, 2020, **267**, 118599.

15. W. R. Erwin, H. F. Zarick, E. M. Talbert and R. Bardhan, *Energy Environ. Sci.*, 2016, **9**, 1577-

1601.

16. V. Etacheri, C. Di Valentin, J. Schneider, D. Bahnemann and S. C. Pillai, *J. Photoch. Photobio. C*, 2015, **25**, 1-29.
17. G. Wang, H. Feng, L. Hu, W. Jin, Q. Hao, A. Gao, X. Peng, W. Li, K. Y. Wong, H. Wang, Z. Li and P. K. Chu, *Nat. Commun.*, 2018, **9**, 2055.
18. L. Hu, C.-C. Fong, X. Zhang, L. L. Chan, P. K. S. Lam, P. K. Chu, K.-Y. Wong and M. Yang, *Environ. Sci. Technol.*, 2016, **50**, 4430-4438.
19. L. Liu and X. Chen, *Chem. Rev.*, 2014, **114**, 9890-9918.
20. J. Schneider, M. Matsuoka, M. Takeuchi, J. Zhang, Y. Horiuchi, M. Anpo and D. W. Bahnemann, *Chem. Rev.*, 2014, **114**, 9919-9986.
21. M. A. Henderson, *Surf. Sci. Rep.*, 2011, **66**, 185-297.
22. M. V. Dozzi and E. Selli, *J. Photoch. Photobio. C*, 2013, **14**, 13-28.
23. R. Asahi, T. Morikawa, T. Ohwaki, K. Aoki and Y. Taga, *Science*, 2001, **293**, 269-271.
24. Y. Liu, W. Shu, K. Chen, Z. Peng and W. Chen, *ACS Catal.*, 2012, **2**, 2557-2565.
25. L. S. Hu, K. F. Huo, R. S. Chen, B. Gao, J. J. Fu and P. K. Chu, *Anal. Chem.*, 2011, **83**, 8138-8144.
26. X. Chen, L. Liu, Y. Y. Peter and S. S. Mao, *Science*, 2011, **331**, 746-750.
27. X. Chen, L. Liu and F. Huang, *Chem. Soc. Rev.*, 2015, **44**, 1861-1885.
28. G. Wang, H. Wang, Y. Ling, Y. Tang, X. Yang, R. C. Fitzmorris, C. Wang, J. Z. Zhang and Y. Li, *Nano Lett.*, 2011, **11**, 3026-3033.
29. J. Qiu, S. Li, E. Gray, H. Liu, Q.-F. Gu, C. Sun, C. Lai, H. Zhao and S. Zhang, *J. Phys. Chem. C*, 2014, **118**, 8824-8830.
30. X. Yu, B. Kim and Y. K. Kim, *ACS Catal.*, 2013, **3**, 2479-2486.

31. H. Lu, B. Zhao, R. Pan, J. Yao, J. Qiu, L. Luo and Y. Liu, *RSC Adv.*, 2014, **4**, 1128-1132.

32. Z. Wang, C. Yang, T. Lin, H. Yin, P. Chen, D. Wan, F. Xu, F. Huang, J. Lin and X. Xie, *Energy Environ. Sci.*, 2013, **6**, 3007-3014.

33. H. Cui, W. Zhao, C. Yang, H. Yin, T. Lin, Y. Shan, Y. Xie, H. Gu and F. Huang, *J. Mater. Chem. A*, 2014, **2**, 8612-8616.

34. A. Sinhamahapatra, J.-P. Jeon and J.-S. Yu, *Energy Environ. Sci.*, 2015, **8**, 3539-3544.

35. M. Ye, J. Jia, Z. Wu, C. Qian, R. Chen, P. G. O'Brien, W. Sun, Y. Dong and G. A. Ozin, *Adv. Energy Mater.*, 2017, **7**, 1601811.

36. H. Tan, Z. Zhao, M. Niu, C. Mao, D. Cao, D. Cheng, P. Feng and Z. Sun, *Nanoscale*, 2014, **6**, 10216-10223.

37. C. Mao, F. Zuo, Y. Hou, X. Bu and P. Feng, *Angew. Chem. Int. Ed.*, 2014, **53**, 10485-10489.

38. K. Zhang, L. Wang, J. K. Kim, M. Ma, G. Veerappan, C.-L. Lee, K.-j. Kong, H. Lee and J. H. Park, *Energy Environ. Sci.*, 2016, **9**, 499-503.

39. L. Liu, Y. Y. Peter, X. Chen, S. S. Mao and D. Shen, *Phys. Rev. Lett.*, 2013, **111**, 065505.

40. H. Liu, K. Tian, J. Ning, Y. Zhong, Z. Zhang and Y. Hu, *ACS Catal.*, 2019, **9**, 1211-1219.

41. H. Zhang, C. Guo, J. Ren, J. Ning, Y. Zhong, Z. Zhang and Y. Hu, *Chem. Commun.*, 2019, **55**, 14050-14053.

42. J. Banfield, *J. Mater. Chem.*, 1998, **8**, 2073-2076.

43. M. Ranade, A. Navrotsky, H. Zhang, J. Banfield, S. Elder, A. Zaban, P. Borse, S. Kulkarni, G. Doran and H. Whitfield, *Proc. Natl. Acad. Sci. USA*, 2002, **99**, 6476-6481.

44. F. Rossella, P. Galinetto, M. Mozzati, L. Malavasi, Y. Diaz Fernandez, G. Drera and L. Sangaletti, *J. Raman Spectrosc.*, 2010, **41**, 558-565.

45. A. Naldoni, M. Allieta, S. Santangelo, M. Marelli, F. Fabbri, S. Cappelli, C. L. Bianchi, R.

Psaro and V. Dal Santo, *J. Am. Chem. Soc.*, 2012, **134**, 7600-7603.

46. R. J. Betsch, H. L. Park and W. B. White, *Mater. Res. Bull.*, 1991, **26**, 613-622.

47. J. Parker and R. Siegel, *Appl. Phys. Lett.*, 1990, **57**, 943-945.

48. T. Mazza, E. Barborini, P. Piseri, P. Milani, D. Cattaneo, A. L. Bassi, C. Bottani and C. Ducati, *Phys. Rev. B*, 2007, **75**, 045416.

49. J. Shen, H. Wang, Y. Zhou, N. Ye, G. Li and L. Wang, *RSC Adv.*, 2012, **2**, 9173-9178.

50. A. Etogo, R. Liu, J. Ren, L. Qi, C. Zheng, J. Ning, Y. Zhong and Y. Hu, *J. Mater. Chem. A*, 2016, **4**, 13242-13250.

51. Y. Cho, S. Kim, B. Park, C. L. Lee, J. K. Kim, K. S. Lee, I. Y. Choi, J. K. Kim, K. Zhang, S. H. Oh and J. H. Park, *Nano Lett.*, 2018, **18**, 4257-4262.

52. J. W. Xue, X. D. Zhu, Y. Zhang, W. D. Wang, W. Xie, J. L. Zhou, J. Bao, Y. Luo, X. Gao, Y. Wang, L. Y. Jang, S. Sun and C. Gao, *ChemCatChem*, 2016, **8**, 2010-2014.

53. F. Xiao, W. Zhou, B. J. Sun, H. Z. Li, P. Z. Qiao, L. P. Ren, X. J. Zhao and H. G. Fu, *Sci. China-Mater.*, 2018, **61**, 822-830.

54. S. G. Ullattil and P. Periyat, *J. Mater. Chem. A*, 2016, **4**, 5854-5858.

55. P. Ramacharyulu, D. B. Nimbalkar, J. P. Kumar, G. Prasad and S.-C. Ke, *RSC Adv.*, 2015, **5**, 37096-37101.

56. S. Misra, S. Andronenko, D. Tipikin, J. Freed, V. Somani and O. Prakash, *J. Magn. Magn. Mater.*, 2016, **401**, 495-505.

57. S. Mohajernia, P. Andryskova, G. Zoppellaro, S. Hejazi, S. Kment, R. Zboril, J. Schmidt and P. Schmuki, *J. Mater. Chem. A*, 2020, **8**, 1432-1442.

58. S. Livraghi, M. Chiesa, M. C. Paganini and E. Giamello, *J. Phys. Chem. C*, 2011, **115**, 25413-25421.

59. S. Kim, Y. Cho, R. Rhee and J. H. Park, *Carbon Energy*, 2020, **2**, 44-53.

60. H. Zhang, J. M. Cai, Y. T. Wang, M. Q. Wu, M. Meng, Y. Tian, X. G. Li, J. Zhang, L. R. Zheng, Z. Jiang and J. L. Gong, *Appl. Catal. B Environ.*, 2018, **220**, 126-136.

61. L. Li, C. Guo, J. Shen, J. Ning, Y. Zhong and Y. Hu, *Chem. Eng. J.*, 2020, **400**, 125925.

62. H. Liu, L. Li, C. Guo, J. Ning, Y. Zhong and Y. Hu, *Chem. Eng. J.*, 2020, **385**, 123929.

63. W. Liu, E. Ha, L. Y. Wang, L. S. Hu, L. Y. S. Lee and K. Y. Wong, *Adv. Mater. Interfaces*, 2018, **5**, 1800611.

Table of Contents

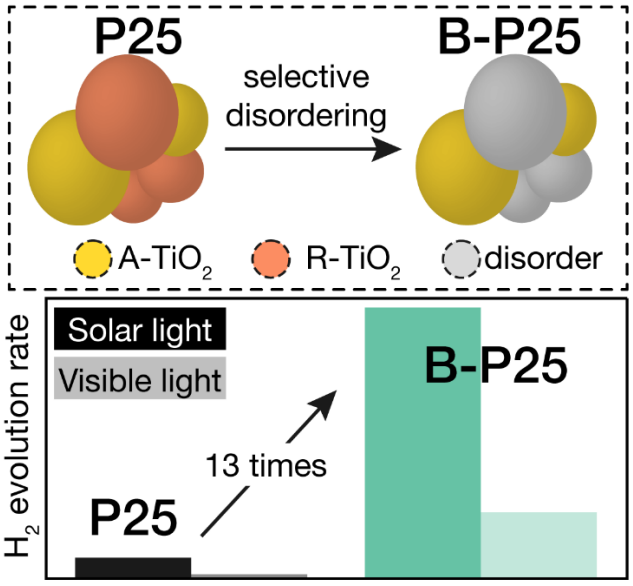

A Janus-type heterojunction between the ordered-anatase and the disordered-rutile phases was fabricated by selectively disordering the rutile phase of commercial P25-TiO_2. The obtained blue order/disorder Janus heterostructure exhibits approximately 13-fold enhancement in photocatalytic H_2 production, compared with the untreated P25-TiO_2.